# Microstructural mechanisms controlling the mechanical behaviour of ultrafine grained martensite/austenite microstructures in a metastable stainless steel

Celada-Casero, C.; Huang, B.M.; Yang, J.-R.; San-Martin, D.

**DOI**
10.1016/j.matdes.2019.107922

**Publication date**
2019

**Document Version**
Final published version

**Published in**
Materials and Design

Materials and Design 181 (2019) 107922

Contents lists available at ScienceDirect

Materials and Design

journal homepage: www.elsevier.com/locate/matdes

# Microstructural mechanisms controlling the mechanical behaviour of ultrafine grained martensite/austenite microstructures in a metastable stainless steel

C. Celada-Casero [a,b,*], B.M. Huang [c], J.-R. Yang [c], D. San-Martin [b]

[a] Delft University of Technology, Department of Materials Science and Engineering, Mekelweg 2, 2628 CD Delft, the Netherlands
[b] Materalia Research Group, Centro Nacional de Investigaciones Metalúrgicas (CENIM-CSIC), Av. Gregorio del Amo 8, 28040 Madrid, Spain
[c] National Taiwan University, Department of Materials Science and Engineering, 1 Roosvelt Road, Section 4, 10617, Taipei, Taiwan

## HIGHLIGHTS

- Increasing the austenitisation temperature reduces similarly the austenite mechanical stability for all heating rates.
- The austenite mechanical stability and work hardening of dual microstructures depend on the strength of martensite.
- Low austenitisation temperatures cause strengthening due to the nanoprecipitation of $Ni_3(Ti,Al)$ in martensite.
- The heating rate barely affects the mechanical properties of microstructures austenitised close to the $A_F$ temperature.

## GRAPHICAL ABSTRACT

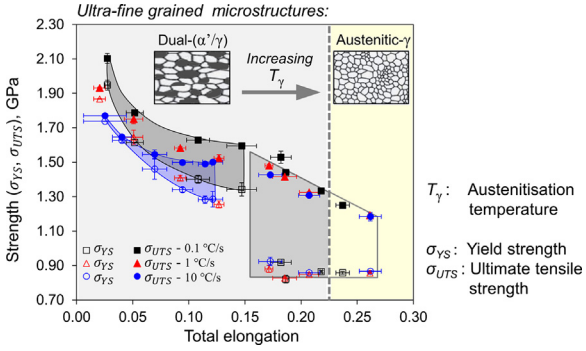


## ARTICLE INFO

*Article history:*
Received 27 April 2019
Received in revised form 31 May 2019
Accepted 7 June 2019
Available online 08 June 2019

*Keywords:*
Strengthening mechanisms
Nano-precipitation
Transformation-induced plasticity
Martensite/austenite microstructures
Metastable stainless steel

## ABSTRACT

This study unravels the microstructural mechanisms controlling the mechanical behaviour and austenite mechanical stability in ultrafine grained austenite/martensite (α′/γ) microstructures, created varying the austenitisation heating rate (0.1–10 °C/s) and temperature within the start-finish austenite formation temperatures ($A_S - A_F$) in a cold-rolled semi-austenitic stainless steel. A wide spectrum of strength-ductility combinations; i.e. strengths of 900–2100 MPa and elongations up to 25%, were characterised by sub-size tensile testing. The nanoprecipitation of $Ni_3(Ti,Al)$ in martensite during heating to low austenitisation temperatures rises the strength, while the martensite recovery, enhanced at low heating rates, improves the work-hardening. The high strength of martensite partially suppresses the formation of mechanically-induced martensite during loading, which is enabled with the increase of austenite volume fraction and contributes positively to the work-hardening. The heating rate barely affects the mechanical properties of microstructures austenitised close to $A_F$. The austenite ultrafine grain size controls the yield strength, while the decrease in austenite mechanical stability and the α′/γ composite effect increase remarkably the work-hardening with respect to dual (α′/γ) microstructures with larger martensite volume fractions and fully austenitised microstructures. These results will enable the design of microstructures with controlled mechanical behaviour for a wider spread use of similar steel grades.



* Corresponding author at: Delft University of Technology, Department of Materials Science and Engineering, Mekelweg 2, 2628CD Delft, the Netherlands.
*E-mail addresses:* c.celadacasero@tudelft.nl (C. Celada-Casero), jryang@ntu.edu.tw (J.-R. Yang), dsm@cenim.csic.es (D. San-Martin).

https://doi.org/10.1016/j.matdes.2019.107922

## 1. Introduction

Semi-austenitic precipitation hardening stainless steels (PHSS) are promising engineering materials suitable for products requiring good corrosion resistance, complex designs and high strength requirements [1,2]. These steels exhibit good formability in the austenitic (γ) annealed state, which is used for shape forming, and transform into martensite (α′) either under the application of stress/strain [3–5] or isothermally, when subjected to cryogenic treatments [6] or high magnetic fields [7,8]. In the martensitic state, the strength can be further increased by precipitation hardening of nano-intermetallic phases [9–12]. This exceptional combination of strength and toughness is a subject of interest for weight reduction in structural applications and for the development of microstructures that enable a wider spread use of these steel grades [13].

Considerable work has been done to improve the mechanical properties of high alloyed stainless steels by adjusting the compositions and heat treatments [14–26]. The focus of most of these works is on the strengthening effects of either multiple precipitation systems during aging treatments after martensite formation [14–17], or the control of the austenite stability and achievement of grain refinement in reversion-treated microstructures [18–22,25,26]. However, the possibility to combine both hardening principles in the microstructure; i.e. precipitation in martensite plus grain-refinement of the austenite with tuned stability, through the adequate adjustment of the processing route is rarely considered. One of the few examples found in the literature is the work of Raabe et al. [27]. Ultrahigh strength steels (1.3–1.5 GPa in ultimate tensile strength) with good ductility (up to 21% of total elongation) are designed by combining partial formation of mechanically-induced martensite, as in conventional TRIP steels, and nanoprecipitation in martensite during aging in low carbon steel, with 9–12 wt. % Mn and minor additions of Ni, Ti and Mo. This evidences the improved mechanical behaviour of high alloyed steels that results from the simultaneous combination of different strengthening mechanisms in martensite/austenite microstructures. However, the complexity of the many microstructural processes involved during the processing of these materials (martensite recovery, precipitation, austenite reversion, grain growth, mechanically-induced martensite formation) makes very difficult to investigate and to control how microstructural modifications might influence their mechanical behaviour.

The present study provides fundamental understanding of the microstructural mechanisms controlling the mechanical behaviour and mechanical stability of austenite on ultrafine grained austenite/martensite microstructures, created under different isochronal austenitisation conditions in a semi-austenitic PHSS. The results of this study will enable the optimisation of processing routes of similar steels for the design of microstructures within a broad window of mechanical properties.

## 2. Material and experimental procedure

### 2.1. Material and creation of microstructures

A metastable semi-austenitic stainless steel of composition 12Cr-9Ni-4Mo-2Cu-1Ti-0.4Al (in wt. %) was investigated. The material was received in the form of cold-rolled sheets of 0.45 mm in thickness (92.5% cold-reduction). The cold-rolled (CR) microstructure mainly consists of deformed martensite phase that contains low volume fractions of the intermetallic χ-phase ($Fe_{36}Cr_{12}Mo_{10}$) (~0.02) and retained austenite (~0.01) [28].

In a previous study, the authors investigated extensively the $\alpha' \rightarrow \gamma$ transformation kinetics by ex-situ magnetisation measurements, EBSD and TEM characterisation in specimens isochronally austenitised in the range of starting-finishing temperatures ($A_S - A_F$) of the martensite-to-austenite ($\alpha' \rightarrow \gamma$) transformation [29], whereas the present paper focus is on characterising and explaining the mechanical behaviour of ultra-fine grained dual martensite/austenite ($\alpha'/\gamma$) and austenitic microstructures based on different microstructural features. In order to do it, ultra-fine grained (UFG) dual martensite/austenite ($\alpha'/\gamma$) and austenitic microstructures were produced by partial and complete austenitisation of the CR material under different heating rates (0.1, 1 and 10 °C/s) to temperatures in the range between the start and finish austenite transformation temperatures ($A_S - A_F$).

Specimens 12 mm long and 4 mm wide were machined with their length perpendicular to the steel rolling direction and were heat treated in the furnace of an Adamel Lomargy DT1000 high-resolution dilatometer operating in a vacuum atmosphere of $10^{-1}$ mbar. Using heating rates of 0.1, 1 and 10 °C/s, the specimens were heated up to different austenitisation temperatures lying in the range $A_S - A_F$. After reaching the target austenitisation temperature, the specimens were quenched to room temperature at a cooling rate of 300 °C/s. A schematic drawing of the thermal treatments is shown in Fig. 1a. The austenite formed during heating does not transform athermally into martensite during quenching to room temperature. In total, eight conditions were created at each heating rate: seven dual martensite/austenite ($\alpha'/\gamma$) microstructures with increasing volume fractions of austenite, produced by heating up below $A_F$, and one fully austenitised microstructure (martensite free), by heating up to $A_F$. Dual ($\alpha'/\gamma$) microstructures will be referred to as dual ($\alpha'/\gamma$)– $\gamma_R$, where $\gamma_R$ represents the volume fraction of reverted austenite.

### 2.2. Characterisation techniques

#### 2.2.1. Scanning electron microscopy

The microstructural characterisation, with focus on determining the composition, size and volume fraction of the intermetallic χ-phase, was performed by scanning electron microscopy (SEM). A field emission gun FEG-SEM Jeol J8M6500, equipped with an Oxford INCA energy dispersive X-ray microanalysis (EDX) system, was used. The specimens were prepared by standard grinding and polishing down to 1 μm using diamond paste. The microstructure was revealed by chemical etching with a hot (60 °C) Lichtenegger-Blöch solution [30]. The quantification of the χ–phase volume fraction and precipitate size was done on SEM micrographs based on the contrast between the particle and the matrix and using the ImageJ image analyser (version 1.47s) [31].

#### 2.2.2. Transmission electron microscopy

Transmission electron microscopes TEM-JEM 2100 HT, operating at 120 kV and a 200 kV high-resolution, and Philips Tecnai-$G^2$-F20 FEI-TEM, which allows for high performance in S/TEM imaging and nanoanalysis, were used. Transmission electron microscopy (TEM) was carried out using the facilities located at the department of Materials Science and Engineering of the National Taiwan University in Taipei, Taiwan. TEM inspection helped to unveil the nature and determine the size of the nanoprecipitates present in the microstructures, as well as to study the size, morphology and distribution of the austenite formed during heating in selected dual ($\alpha'/\gamma$) microstructures.

Discs of 3 mm in diameter were machined from dilatometry specimens by wire erosion. Thin foils were prepared from these discs by mechanical grinding down to about 30 μm in thickness and subsequent electropolishing with a 10/90 perchloric/acetic acid solution, at 17 °C and 38 V, using a twin-jet Struers Tenupol-5.

#### 2.2.3. Electron probe microanalysis

A JEOL JXA 8900 M microprobe equipped with a wavelength dispersive spectrometer (WDS) was used to map the chemical segregation present along the cross-section of the steel thickness after heating up to 850 °C at 0.1 °C/s. A step size of 1 μm was employed. Specimen preparation was done in the same manner as for SEM.

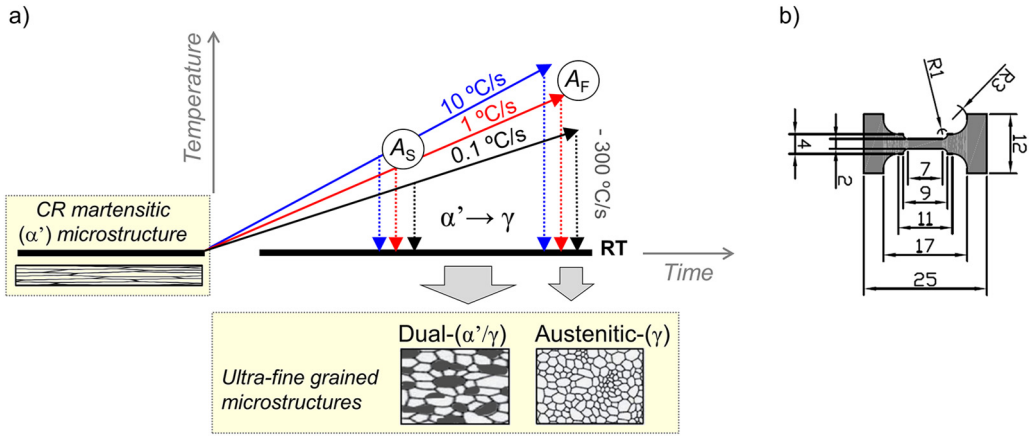


**Fig. 1.** (a) Schematic drawing of the isochronal austenitisation heat treatments and resulting microstructures. $A_s$ and $A_F$ stand for the start and finish martensite (α′) to austenite (γ) transformation temperatures, respectively; (b) Sub-size tensile test specimen dimensions (in millimetres).

*2.2.4. Tensile tests*

The mechanical response of the UFG dual (α′/γ) and austenitic microstructures was investigated by tensile tests done on sub-size specimens (see dimensions in Fig. 1b). Sub-size specimens were machined out of the CR material by wire erosion, with the gage length perpendicular to the steel rolling direction, and heat-treated in the furnace of a LK02 dilatometer. Tensile experiments were carried out until fracture in a universal tensile testing machine with a load cell of 10 kN, at room temperature, and applying a strain rate of $\dot{\varepsilon} = 5 \times 10^{-4}$ $s^{-1}$. At least two tensile tests were conducted per condition to study the reproducibility.

*2.2.5. Magnetisation measurements*

Magnetisation saturation measurements were used to determine the austenite/martensite volume fractions and, indirectly, investigate the mechanical stability of the austenite present in the austenitised microstructures. Using a quantum design MPMS-XL SQUID magnetometer present at CAI of Physical Techniques of the Complutense University of Madrid, the magnetisation saturation of the whole gauge length of the tensile specimens after fracture, $M_{sat}$, was measured at room temperature. The martensite volume fraction induced during tensile loading was calculated from: $f_{\alpha'} = M_{sat}/M_{sat}{}^{\alpha'}$, where $M_{sat}{}^{\alpha'}$ represents the saturation magnetisation of pure martensite and yields 146 $Am^2/kg$, as described in a previous work [5].

## 3. Results

*3.1. Creation of ultrafine grained dual (α′/γ) and austenitic microstructures*

Fig. 2 shows the evolution of the volume fraction of austenite (solid data points) and χ-phase (open data points) with the austenitisation temperature upon the investigated isochronal conditions (0.1, 1 and 10 °C/s). According to our previous study [29], the α′ → γ transformation proceeds in two steps as a consequence of the chemical banding present in the CR material [28]. Compositional variations of more than 2 wt. % in Ni and Cr were detected by electron probe microanalysis (EPMA) after mapping the whole steel sheet thickness [28]. The inhomogeneous distribution of alloying elements in bands results in martensite with different thermal stabilities across the steel thickness of the initial CR microstructure. The martensite that belongs to Ni-rich (Cr-poor) bands is less stable upon heating than the martensite within Ni-poor (Cr-rich) bands and, thus, it transforms into austenite at lower temperatures than the martensite within Ni-poor bands. This creates a two-step α′ → γ transformation kinetic curve that is observed for all heating rates.

Table 1 displays the $A_S - A_F$ temperatures and the austenite grain size (AGS) of fully austenitised microstructures as a function of the heating rate, which were reported in [29]. With increasing heating rates, the α′ → γ transformation temperatures shift to higher values, which is characteristic of diffusional processes [32]. The volume fraction of χ-phase rises as the austenitisation temperature increases, especially upon 0.1 °C/s, and reaches the maximum volume fraction in fully austenitised microstructures, heated up to $A_F$. Therefore, fully austenitic microstructures consist of an austenitic matrix with grain sizes in the sub-micrometre range (Table 1) and a volume fraction of χ-phase of about 0.10 or lower, depending on the heating rate (Fig. 2).

*3.2. Characterisation of intermetallic phases in selected dual (α′/γ) microstructures*

Two different intermetallic phases were identified to form during continuous heating in the steel under investigation: the $Ni_3(Ti,Al)$ phase and the χ-phase.

*3.2.1. The $Ni_3(Ti,Al)$ phase*

The precipitation of hardening nano-sized intermetallic phases involving Ni, Ti, Al, Cu or Mo in martensite is representative of PHSSs

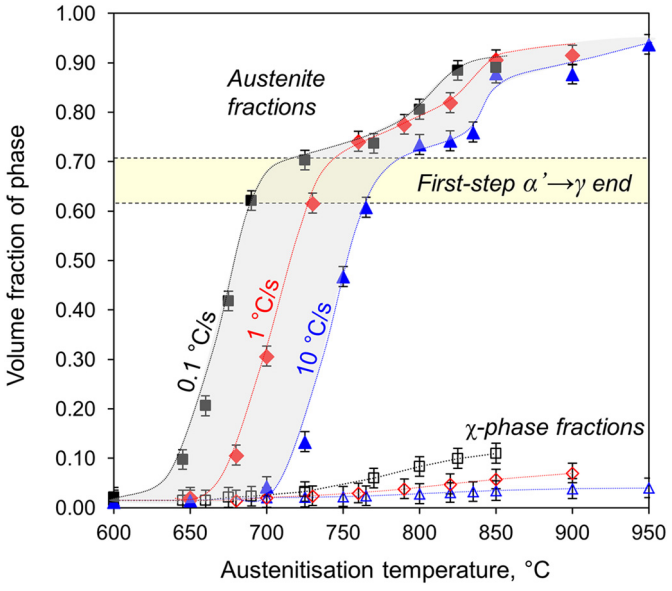


**Fig. 2.** Evolution of austenite and χ–phase volume fractions with the austenitisation temperature and heating rate. Dotted lines are plotted as a guide for the eye.

**Table 1**
Starting ($A_S$) and finishing ($A_F$) martensite-to-austenite transformation temperatures per heating rate (HR). Austenite grain size (AGS) of fully austenitised microstructures heated up to $A_F$ [29].

| *HR* (°C/s) | $A_S$ (°C) | $A_F$ (°C) | *AGS* (nm) |
|---|---|---|---|
| 0.1 | 600 ± 25 | 825 ± 12 | 440 ± 240 |
| 1 | 650 ± 15 | 900 ± 25 | 430 ± 260 |
| 10 | 680 ± 12 | 950 ± 25 | 360 ± 200 |

**Table 2**
Average length ($l$) and width ($w$) of the $Ni_3$(Ti,Al) rod-like nanoprecipitates present in dual $(\alpha'/\gamma) - \gamma_R = 0.10$ and dual $(\alpha'/\gamma) - \gamma_R = 0.50$ microstructures obtained by heating at 0.1 and 10 °C/s up to different austenitisation temperatures ($T_\gamma$).

| Dual $(\alpha'/\gamma) - \gamma_R$ | *HR* (°C/s) | $T_\gamma$(°C) | $l$ (nm) | $w$ (nm) |
|---|---|---|---|---|
| 0.10 | 0.1 | 650 | 28 ± 11 | 11 ± 3 |
| | 10 | 725 | 14 ± 12 | 6 ± 4 |
| 0.50 | 0.1 | 680 | 27 ± 5 | 14 ± 3 |
| | 10 | 750 | 17 ± 6 | 7 ± 3 |

and usually occurs in the range from 300 °C to 550 °C [9,11,12]. Therefore, these phases precipitate in martensite during continuous heating before the formation of austenite and, thus, below $A_S$. Fig. 3 shows a BF- and a high-resolution (HR-) TEM micrographs of the martensitic matrix of dual $(\alpha'/\gamma)-0.10$ microstructures obtained by heating at 0.1 and 10 °C/s up to 650 and 725 °C, respectively. Rod-shaped particles in the nanometre scale can be distinguished. Their identification is more difficult in the microstructure heated at 10 °C/s, as the precipitates are smaller, their volume fraction is lower and the martensite recovery is less pronounced than after heating at 0.1 °C/s. The BF and HR-TEM images of Fig. 3a show that the precipitates grow along two preferred directions, with their axial length parallel to the $[011]_{\alpha'}$ direction. The compositional Energy Dispersive Spectroscopy (EDS) microanalysis of the particles in the HR-TEM image shows high contents of Ni, Ti and Al compared to those of the nominal composition and suggests a stoichiometry that corresponds to the intermetallic $Ni_3$(Ti,Al) phase [33]. The clear identification of the $Ni_3$(Ti,Al) nanoprecipitates by means of TEM is difficult, particularly in microstructures heated at 10 °C/s, due to diffraction contrast effects that may arise from the thin-foil thickness and the strain contrast from dislocations and crystalline orientation of the precipitates. HRTEM allows the precipitate size to be determined more accurately than TEM; however, the number of particles that can be analysed in this way is low for statistical purposes. Nevertheless, in order to roughly estimate the size evolution of the $Ni_3$(Ti,Al) precipitates during heating at different rates, the length and width of the $Ni_3$(Ti,Al) precipitates were measured on HRTEM and TEM micrographs of dual $(\alpha'/\gamma)-0.10$ and dual $(\alpha'/\gamma)-0.50$ microstructures, obtained by heating at 0.1 and 10 °C/s to the austenitisation temperatures ($T_\gamma$) displayed in Table 2. The results are presented as the mean and standard deviation values of the length ($l$) and the width ($w$). The microstructures heated at 0.1 °C/s exhibit somewhat larger precipitates than the microstructures austenitised at 10 °C/s. This is to be expected since slow heating rates provide a longer time for the diffusion of the substitutional elements, and thus for precipitate growth, compared to faster heating rates. In contrast, the increase of the austenitisation temperature barely influences the precipitate size, as it can be observed by comparing the dual $(\alpha'/\gamma)-0.10$ and dual $(\alpha'/\gamma)-0.50$ microstructures for each heating rate (Table 2).

### 3.2.2. The χ-phase

The χ-phase ($Fe_{36}Cr_{12}Mo_{10}$) is an intermetallic that forms in high-molybdenum stainless steels in the range from 600 to 900 °C [34]. Therefore, the formation of χ-phase occurs simultaneously with the martensite-to-austenite transformation during continuous heating (Fig. 2). Fig. 4 shows the characterisation by TEM of the χ-phase present in fully austenitised microstructures obtained upon heating at 0.1 and 10 °C/s to $A_F$, 825 °C and 950 °C, respectively. The high-angle annular dark-field scanning transmission electron microscopy (HAADF-STEM) micrograph in Fig. 4a (left) reveals the compositional contrast between the austenitic matrix and the χ-phase based on the atomic number. The higher the atomic number of the elements constituting a phase, the brighter the signal. The high Mo content in the χ-phase, as the EDS microanalysis of the bright-field (BF) TEM micrograph confirms, makes the χ-phase much brighter than the matrix. Two different sizes of χ-phase were identified. Particles as large as 1 μm were present in the cold-rolled microstructure and were originated during the solidification of the steel [5]. Particles in the nanometre scale; i.e. of 150 nm or lower depending on the heating rate, precipitate during the isochronal austenitisation, mainly at austenite grain boundaries and triple junctions at low heating temperatures above $A_S$, and also intragranularly at temperatures close to $A_F$.

### 3.3. Mechanical behaviour of dual $(\alpha'/\gamma)$ and austenitic microstructures

Fig. 5 shows the engineering stress-plastic strain ($\sigma_e - \varepsilon_e$) curves of all UFG dual $(\alpha'/\gamma)$ and austenitic microstructures obtained by isochronal austenitisation up to temperatures within $A_S - A_F$. The tensile behaviour of the cold-rolled microstructure (CR) is included for comparison. Similar trends are observed for all heating rates. Microstructures austenitised slightly above $A_S$ (645, 680 and 715 °C, resp. to 0.1, 1 and 10 °C/s) exhibit an increase of yield and tensile strength compared to the CR microstructure. Further rise of the austenitisation temperature decreases the strength and increases the elongation. It is eye-catching the significant yield strength drop observed at intermediate austenitisation temperatures, coinciding with the end of the first-step of the $\alpha' \rightarrow \gamma$ transformation indicated in Fig. 2 by a yellow ribbon. The yield strength drop is accompanied by a significant increase of

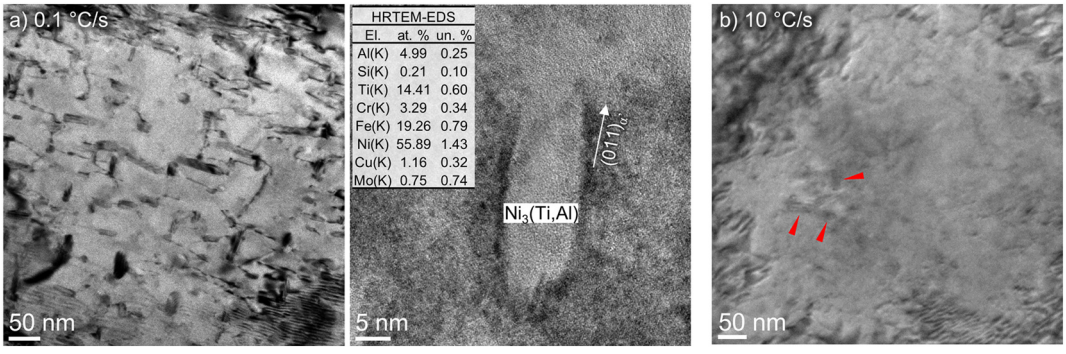


**Fig. 3.** BF TEM micrographs of the martensitic matrix of dual $(\alpha'/\gamma)$ – 0.10 microstructures obtained at (a) 0.1 °C/s to 650 °C and (b) at 10 °C/s to 725 °C. Rod-shaped nanometric $Ni_3$(Ti,Al) precipitates can be distinguished. In (a), HRTEM micrograph and microanalysis of the precipitate.

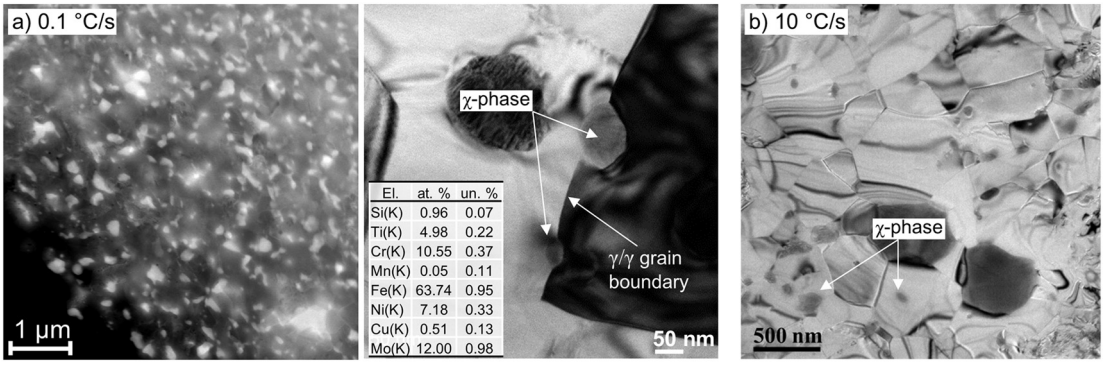


**Fig. 4.** (a) HAADF-STEM (left) and BF-TEM (right) micrographs with EDS microanalysis of a χ-phase particle; and (b) BF-TEM micrograph of the austenitic microstructures obtained at 825 °C upon 0.1 °C/s (a) and at 950 °C upon 10 °C/s (b), respectively.

work-hardening, as the difference between the maximum tensile strength and the yield strength indicates. Further increase of the austenitisation temperatures reduces moderately the work-hardening ability while sustaining similar yield strengths. The microstructures austenitised to $A_F$ or slightly below present a sudden drop of strength just after the yield point (yield drop) followed by a yield point elongation. During the yield point elongation, the deformation proceeds at a constant stress level until values of $\varepsilon_e$~0.05, after which the strength increases. The microstructures austenitised to $A_F$ present the largest elongation values.

### 3.4. Mechanical stability of the austenite

Fig. 6 represents the volume fraction of mechanically-induced martensite after fracture against the initial volume fraction of austenite present in the microstructure before testing ($\gamma_R$) for partial and fully austenitised microstructures. Fixed volume fractions of untransformed austenite after fracture ($\gamma_{un}$) are indicated by dashed lines as a guide to the eye. The comparison of these lines with the experimental data shows that, irrespective of the heating rate, similar volume fractions of $\gamma_{un}$ remain after fracture for microstructures with similar initial austenite volume fractions. This indicates that the mechanical stability of the austenite is not much influenced by the heating rate and decreases with increasing austenitisation temperatures. Microstructures austenitised just above $A_S$, i.e. $\gamma_R$= 0.10, have the highest mechanical stability since no martensite is induced after tensile deformation. Microstructures with the austenite volume fractions up to around 0.45–0.50 exhibit a quite stable austenite as well, given that retain the largest volume fractions of untransformed austenite ($\gamma_{un} \approx 0.30$). Increasing $\gamma_R$ above 0.50 results in a continuous decrease of the $\gamma_{un}$ and, thus, austenite mechanical stability. Eventually, the martensitic transformation is almost complete in fully austenitised microstructures, particularly for the condition heated at 0.1 °C/s, whose $\gamma_{un} \approx 0$.

## 4. Discussion

### 4.1. The influence of the austenitisation temperature on the mechanical stability of austenite

Fig. 6 has shown that the mechanical stability of the austenite in partially and fully austenitised microstructures decreases with the increase of austenitisation temperature and, thereby, with the austenite volume fraction. This observation is roughly independent of the austenitisation heating rate. The stability of the austenite is mainly controlled by the grain size [35], the chemical composition [36] and the stress/strain partitioning during loading [37,38]. In the steel under investigation, the inhomogeneous distribution of the alloying elements in bands parallel to the steel sheet rolling-direction, observed in the initial microstructure [28], will influence significantly the thermal/mechanical stability of the austenite present in these microstructures. Fig. 7 shows EPMA line scans of Ni, Cr and Cu across the whole steel sheet thickness after austenitisation at 0.1 °C/s up to 850 °C (slightly above $A_F$ for this heating rate). The composition has been normalized by the nominal composition of each element, which is indicated by the horizontal dashed line. This result shows that, even after slow heating to 850 °C, the chemical banding present in the initial microstructure persists [29]. The locations with positive segregation of Ni and Cu (austenite stabilising elements) coincide with negative segregation of Cr (ferrite stabilising element). Thus, in the initial cold-rolled microstructure, the bands with the maximum Ni/Cu contents represent martensitic regions

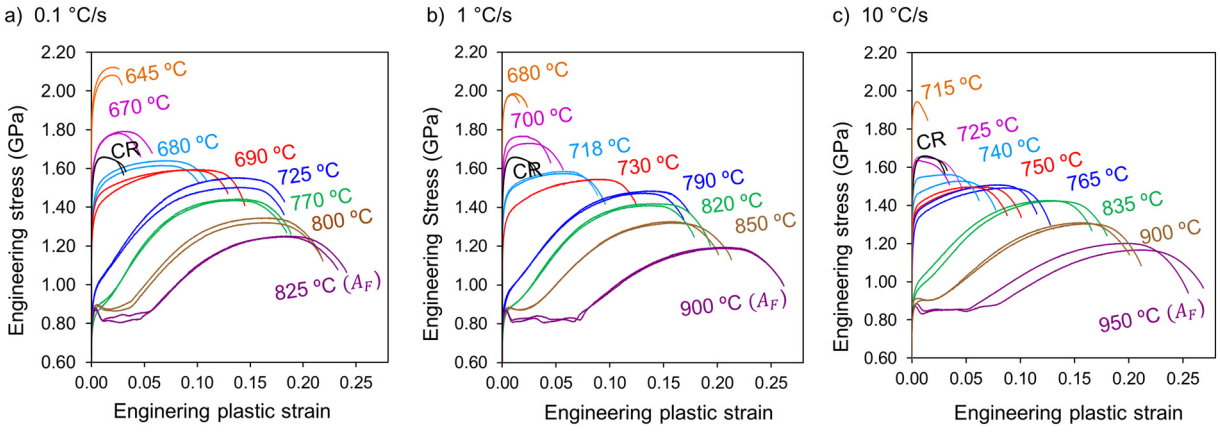


**Fig. 5.** Engineering stress-plastic strain curves of UFG dual (α′/γ) and austenitic microstructures obtained upon different isochronal conditions: (a) 0.1 °C/s; (b) 1 °C/s and (c) 10 °C/s. The austenitisation temperature is indicated. The curve of the CR condition is included for comparison. For colour interpretation, the reader is referred to the web version of this article.

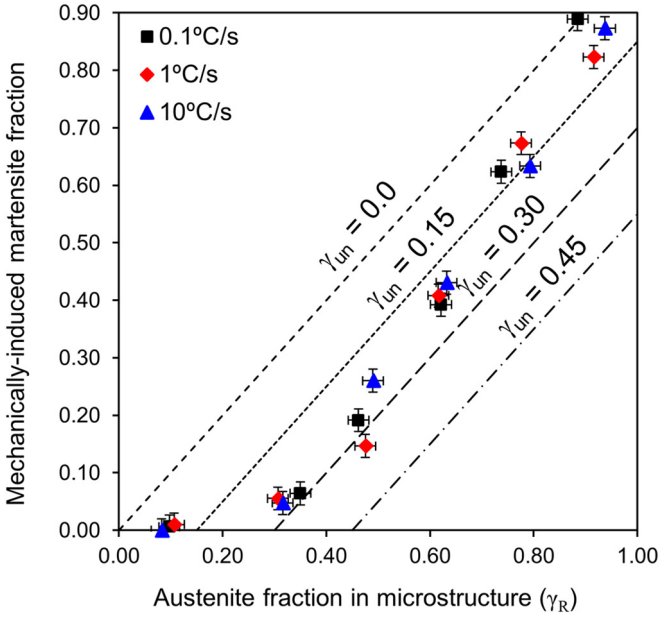


**Fig. 6.** Volume fraction of mechanically-induced martensite after fracture as a function of the austenite volume fraction present in the dual ($\alpha'/\gamma$) or fully austenitised microstructures ($\gamma_R$). Dashed lines represent fixed values of untransformed austenite volume fractions after fracture ($\gamma_{un}$).

with the lowest thermal stability and thus the lowest $A_S$ (coloured in yellow in Fig. 7). It has previously observed by SEM and EBSD that the austenite nucleates and grows first at these locations during heating [29]. Therefore, the austenite of dual ($\alpha'/\gamma$)$-\gamma_R \leq 0.10$ microstructures forms within these Ni-rich (Cr-poor) bands and exhibits the highest mechanical stability. Further heating to higher austenitisation temperatures involves the transformation of bands with increasing $A_S$ and, eventually, of the Ni-poor (Cr-rich) bands with the highest $A_S$. Following this line of though, the overall mechanical stability of the austenite in dual ($\alpha'/\gamma$) microstructures would decrease with the rise of the austenite volume fraction. The last bands to transform to austenite during heating would be the first to transformed to martensite during mechanical loading due to their high-Cr, low-Ni content.

To elucidate if the compositional variations due to chemical banding could be responsible for the decrease of austenite mechanical stability with the increase of austenite volume fraction in dual ($\alpha'/\gamma$) microstructures (Fig. 6), thermodynamic calculations of the chemical driving force at room temperature; i.e. molar Gibbs free energy difference between austenite and martensite ($\Delta G_{chem}^{\gamma\rightarrow\alpha} = G^{\alpha} - G^{\gamma}$), were performed by ThermoCalc software (TCFE9 database). The results are displayed in Table 3 for the nominal composition and the maximum and minimum Ni contents as quantified in Fig. 7, Ni-rich and Ni-poor, respectively. Compared to the nominal composition, the higher and lower $\Delta G_{chem}^{\gamma\rightarrow\alpha}$ values of the Ni-rich and Ni-poor bands indicate a higher and a lower austenite stability, respectively. As proposed by Patel and Cohen [39], the formation of mechanically-induced martensite is possible when the combination of mechanical ($\Delta G_{mech}$) and chemical ($\Delta G_{chem}^{\gamma\rightarrow\alpha}$) driving forces is lower than the critical driving force needed to initiate the transformation: $\Delta G_{cr}^{\gamma\rightarrow\alpha} \geq \Delta G_{chem}^{\gamma\rightarrow\alpha} + \Delta G_{mech}$. Therefore, the negative/positive increment of $\Delta G_{mech}$ required to initiate the transformation within Ni-rich/Ni-poor bands should be at least equal to the difference between the $\Delta G_{chem}^{\gamma\rightarrow\alpha}$ value of the nominal composition and that of the Ni-rich/Ni-poor bands (represented by $\Delta G_{mech}^{rel}$ in Table 3). In uniaxial tension, the contribution to the mechanical driving force is proportional to the macroscopic applied stress ($\sigma$) as: $\Delta G_{mech} = -0.822\sigma$ J/mol, as derived by Olson et al. [40]. Substitution of $\Delta G_{mech}^{rel}$ in Olson's equation yields the difference in critical stress, with respect to the nominal composition, needed to initiate the martensitic transformation within Ni-rich/Ni-poor bands, which is represented as $\Delta\sigma_{cr}^{rel}$ in Table 3. This analysis reveals that the $\gamma \rightarrow \alpha'$ transformation within the Ni-rich bands requires a higher mechanical driving force and, thus, a higher critical applied stress (83 MPa), than the transformation of austenite with nominal composition. In contrast, Ni-poor austenite transforms at lower critical applied stress (−93 MPa) than the austenite with the nominal composition, represented by the minus sign in Table 3. Nevertheless, with respect to the nominal composition, these small variations in the critical applied stress induced by the chemical banding (about ±100 MPa) do not explain satisfyingly the results of Fig. 6. The mechanical characterisation of partially and fully austenitised microstructures gives a spectrum of yield strengths of 900–1950 MPa (Fig. 5), which represents a range of mechanical driving forces of 740–1600 J/mol. These values are well above the 400 J/mol calculated as critical to mechanically induce the formation of martensite in the steel under investigation by Geijselaers & Perdahcioğlu [41,42]. In their works, the steel had been austenitised at 1050 °C for 30 s and slowly cooled down to room temperature, resulting in a fully austenitic microstructure of average grain size of 6 μm, as characterised previously by San-Martin et al. [6]. Therefore, compared to the findings by Geijselaers & Perdahcioğlu, the higher mechanical stability of the austenite in dual ($\alpha'/\gamma$) and fully austenitic microstructures investigated in the present work might be attributed to the ultra-fine austenite grain size, as also found before in multiphase steels [35]. The decrease in the austenite mechanical stability as the austenite volume fraction in the microstructure increases is not explained by the sole presence of the chemical banding in the cold-rolled microstructure. The role of

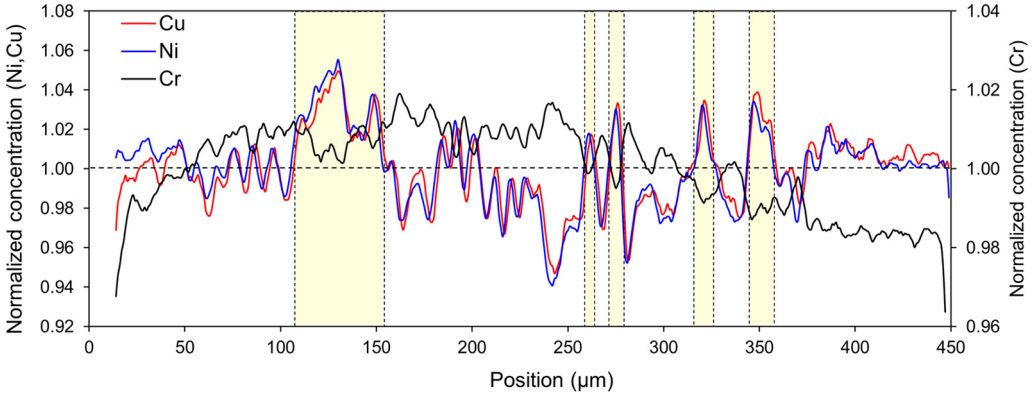


**Fig. 7.** EPMA line scans of Ni, Cu and Cr along the steel-sheet thickness after complete austenitisation at 0.1 °C/s to 850 °C. The concentration is normalized with the nominal composition for each element.

**Table 3**
Compositional dependence of the chemical driving force ($\Delta G^{\gamma\to\alpha}_{chem}$). The mechanical driving force and critical applied stress, relative to the nominal composition of the steel, required to initiate the martensite formation at room temperature are represented by $\Delta G^{rel}_{mech}$ and $\Delta\sigma^{rel}_{cr}$, respectively.

| (wt. %) | Cr | Ni | Cu | Ti | $\Delta G^{\gamma\to\alpha}_{chem}$ (J/mol) | $\Delta G^{rel}_{mech}$ (J/mol) | $\Delta\sigma^{rel}_{cr}$ (MPa) |
|---|---|---|---|---|---|---|---|
| Nominal | 12.00 | 8.87 | 1.91 | 1.35 | −3116 | | |
| Ni-rich | 12.05 | 9.30 | 2.00 | 1.53 | −3048 | −68 | 83 |
| Ni-poor | 12.23 | 8.30 | 1.82 | 1.15 | −3195 | 79 | −93 |

additional factors in the variation of the austenite mechanical stability, as the inhomogeneous distribution of stresses/strains during loading among the constituent phases [37,38], will be discussed in the next section.

### 4.2. Strengthening mechanisms of UFG dual ($\alpha'/\gamma$) and austenitic microstructures

Fig. 8a shows the evolution of the 0.2% offset yield strength ($\sigma_{YS}$, open dots) and the ultimate tensile strength ($\sigma_{UTS}$, solid dots) with the volume fraction of austenite for the three isochronal austenitisation conditions investigated (different colours are used for each heating rate). Similarly, Fig. 8b shows the evolution of the uniform and total elongation with the volume fraction of austenite. The values obtained for the cold-rolled material are included for comparison as triangles pointed out by arrows and labelled as (CR). Based on the evolution of the strength, three regions can be identified in Fig. 8a. Region ① is characterised by a strength increment of dual ($\alpha'/\gamma$)−$\gamma_R \le 0.10$ microstructures with respect to the CR state. In region ②, increasing the austenite volume fraction above 0.10 causes a continuous decay in the yield strength and tensile strength. Further austenite formation above 0.60 drops the yield strength in about 400 MPa, setting the beginning of region ③. Thereafter, the yield strength remains essentially constant and the tensile strength decreases linearly with further increase of the austenite volume fraction in the microstructure. The trend is similar for all heating rates. In contrast to the more complex behaviour of the strength, Fig. 8b shows that the elongation increases continuously with the rise of austenite volume fraction in the microstructure. This dependency is quasi-linear for austenite volume fractions above 0.60. The heating rate barely influences the elongation behaviour, although some scatter is observed around the solid/dashed lines drawn in these plots as a guide to the eye. The influence of the main microstructural parameters behind this mechanical behaviour is discussed in the following sections. For this purpose, the microstructures have been classified as *microstructures with a martensitic matrix* and *microstructures with an austenitic matrix*, depending on the predominant matrix phase.

#### 4.2.1. Microstructures with a martensitic matrix

*A) Nano-precipitation of $Ni_3(Ti,Al)$ in martensitic matrix.*

Fig. 8a shows that the strength of dual ($\alpha'/\gamma$)−$\gamma_R \le 0.10$ microstructures increases with respect to the cold-rolled state (region ①) and that lowering the heating rate increases the peak strength and the work hardening ability; i.e. the difference between tensile and yield strengths. On the one hand, this more pronounced yield strength increase obtained by lowering the heating rate is attributed to the formation of larger volume fractions of nanosized rod-shaped $Ni_3(Ti,Al)$ particles in the martensitic matrix, as characterised by TEM (Fig. 3) and also observed in similar steels [16]. On the other hand, the improved work-hardening ability might depend directly on the increase in the mobile dislocation density and the effective dislocation mean free path in martensite during heating [43], given that dual ($\alpha'/\gamma$)−$\gamma_R \le 0.10$ microstructures do not exhibit mechanically-induced martensite after fracture (Fig. 6). The role of the heating rate in the yield strength and work-hardening ability of dual ($\alpha'/\gamma$) microstructures within region ① is discussed in the following paragraphs.

*Yield strength.*

Contrary to carbon steels, the high strength of martensite in the CR state of this ultra-low carbon steel (<0.01 wt.% C) relies on the solid solution hardening effect of substitutional alloying elements and on the high density of dislocations forests generated during cold-rolling, as found also for other ultra-low carbon martensitic steels [44]. However, in the steel under investigation, the strength can be further increased by precipitation hardening during an aging treatment at temperatures around 475 °C [9,11,12,45]. The strengthening due to particle-

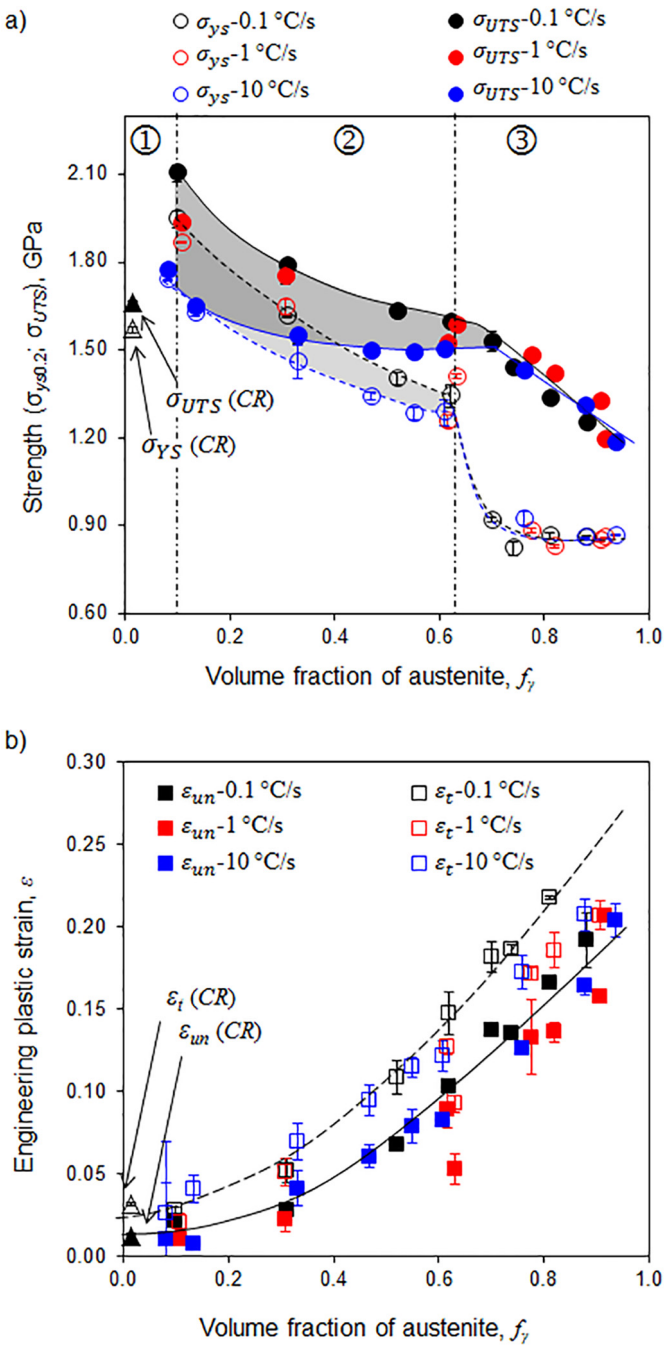


**Fig. 8.** Dependency of (a) the yield strength and ultimate tensile strength ($\sigma_{ys}$, $\sigma_{UTS}$) and (b) the uniform and total elongation ($\varepsilon_{un}$, $\varepsilon_t$) with the austenite volume fraction in UFG dual ($\alpha'/\gamma$) and fully austenitised microstructures. Solid and dashed lines are drawn as guides to the eye. For colour interpretation, the reader is referred to the web version of this article.

dislocation interaction is described by the Orowan mechanism [46]. The applied stress required for dislocations to bypass spherical precipitates ($\sigma_{ppt}$) depends on the volume fraction ($f_{ppt}$) and the size of precipitates:

$$\Delta\sigma_{ppt} = \left(\frac{0.538\mu b\left(f_{ppt}\right)^{1/2}}{X}\right)\ln\left(\frac{X}{2b}\right) \quad (1)$$

where $\mu$= 80,000 MPa is the shear modulus, $b$= 0.286 nm is the magnitude of the Burgers vector and $X$ is the precipitate equivalent spherical diameter, which can be calculated based on the precipitate area of the rod-shaped $Ni_3$(Ti,Al) particles. In addition to the precipitation hardening effect, it has to be considered that the precipitation process also reduces the content of alloying elements in solid solution in the matrix ($x_i^{\alpha'}$) according to:

$$x_i^{\alpha'} = \left(x_i^{Alloy} - x_i^{ppt} f_{ppt}\right)/\left(1 - f_{ppt}\right) \quad (2)$$

where $x_i$ is the content of element $i$ in at. %. Therefore, the solid solution strengthening ($\sigma_{ss}$), which accounts for the lattice distortions and local changes in the elastic modulus due to the presence of an element $i$ with respect of Fe, reduces as well as [17]:

$$\Delta\sigma_{ss} = \sum_i \left(\beta_i^2 x_i^{\alpha'}\right)^{1/2} \quad (3)$$

where $\beta_i$ is the solid solution strengthening coefficient (Table 4) and $x_i^{\alpha'}$ is the composition of the martensite phase in at.%.

To study the influence of the heating rate on the yield strength of dual ($\alpha'/\gamma$)−$\gamma_R$ ≤ 0.10 microstructures, the strengthening contribution due to the nanoprecipitation of $Ni_3$(Ti,Al) has been analysed. As a first approximation, it is assumed that the increase in the overall yield strength of dual ($\alpha'/\gamma$)−$\gamma_R$ ≤ 0.10 microstructures ($\sigma_{YS}^{(\alpha'/\gamma)-0.10}$) is mainly due to precipitation hardening and, thus, the contribution of the small volume fraction of austenite ($\gamma_R$ ≤ 0.10), the decrease in solid solution strengthening due to the nanoprecipitation of $Ni_3$(Ti,Al) and the martensite recovery (reduction in the contribution from dislocations forests during heating) could be neglected:

$$\sigma_{YS}^{(\alpha'/\gamma)-0.10} \approx f_{\alpha'}\left(\sigma_{YS}^{\alpha'-CR} + \Delta\sigma_{ppt}\right) \quad (4)$$

where $f_{\alpha'}$ (=0.90) is the martensite volume fraction and $\sigma_{YS}^{\alpha'-CR}$ is the experimentally measured yield strength of the martensite in the CR state. Substitution of Eq. (1) in Eq. (4) allows the volume fraction of precipitates to be estimated. Additionally, knowing this volume fraction, the mean spacing between particles (λ) is determined as $\lambda = 4X/6f_{ppt}$ [46]. The results are displayed in Table 5 for the heating rates of 0.1 and 10 °C/s. The $f_{ppt}$ values obtained seem reasonable since a similar volume fraction of $Ni_3$(Ti,Al) precipitates (around 0.05) is predicted in equilibrium with bcc-iron in the range from room temperature to 575 °C by ThermoCalc software (TCFE9 database). Taking into account the calculated $f_{ppt}$ and the $Ni_3$(Ti,Al) compositional analysis by EDS-TEM (Fig. 3), Eq. (3) allows to estimate the reduction in the solid solution strengthening ($\Delta\sigma_{ss}$) of martensite due to the formation of $Ni_3$(Ti,Al). After heating at 0.1 and 10 °C/s, the formation of these nanoprecipitates reduces $\Delta\sigma_{ss}$ in about 99 MPa and 25 MPa, respectively, with respect to that in the CR state ($\sigma_{ss}$= 580 MPa). These values are relatively small compared to the precipitation hardening ($\Delta\sigma_{ppt}$) values, which makes reasonable the aforementioned assumption.

**Table 4**
Solid solution strengthening coefficients [17].

| Element | Cr | Ni | Mo | Cu | Ti | Al | Mn |
|---|---|---|---|---|---|---|---|
| β (MPa/at.%) | 622 | 708 | 2362 | 320 | 2628 | 196 | 540 |

It was observed by atom probe tomography that $Ni_3$(Ti,Al) precipitates form in direct contact with Cu/Ni/Al/Ti-rich clusters within the first 5 min of aging at 475 °C [9,11,45]. A high density of dislocation forests in the CR microstructure provides a high number density of precipitates within the first few hours of isothermal holding. This causes a continuous hardening effect that raises the strength in about 1 GPa after 72 h of aging 450 °C [12]. A significant hardness increase, of more than 100 HV, was also detected in microstructures heated up at 100 °C/s to 650 °C in the steel under investigation [29]. Although $Ni_3$(Ti,Al) precipitates were not observed by TEM in this case, the hardness increase evidences the likely rapid atom cluster formation kinetics in just a few seconds. It is well known that the presence of these clusters/precipitates retard the process of dislocations annihilations during heating. It has been experimentally observed that this retardation is more pronounced the faster the heating rate is [29]. Therefore, it is reasonable to expect the recovery of dislocation forests during heating up to temperatures around $A_S$ to be very scarce. In addition, it is important to bear in mind that, on the one hand, $f_{ppt}$ might be underestimated since the decrease in solid solution and dislocation density are not considered by Eq. (4), even if their strengthening contribution is small compared to the precipitation hardening. Besides, given the small precipitate size and difficulty in detecting them by TEM and HR-TEM, it is very hard to determine their size accurately and, thus, $f_{ppt}$ might be underestimated or overestimated. The EDS-TEM compositional microanalysis of the martensitic matrix in the dual ($\alpha'/\gamma$)−$\gamma_R$ ≤ 0.10 microstructure heated up at 0.1 °C/s yields Ni contents of 5.0 ± 0.4 at.%. The substitution of this value in Eq. (2) results in $f_{ppt}$ = 0.05 ± 0.01, which is very close to the value calculated in Table 5. In summary, it can be said that martensite softening due to the decrease in solid solution and recovery during heating is much smaller than the hardening due to the nanoprecipitation of $Ni_3$(Ti,Al) in martensite, which is the main strengthening mechanism in dual ($\alpha'/\gamma$)−$\gamma_R$ ≤ 0.10 microstructures.

*Work-hardening.*

Since dual ($\alpha'/\gamma$)−$\gamma_R$ ≤ 0.10 microstructures do not exhibit mechanically-induced martensite after fracture (Fig. 6), the work-hardening rate would depend on the increase in the mobile dislocation density in the martensite with time upon the applied stress (to comply with the imposed strain rate) and on the effective dislocation mean free path, which determines the mean slip length before the dislocation is annihilated or immobilised [43]. The dislocation mean free path is given by the mean spacing between pinning points such as dislocations, precipitates and grain boundaries. According to the interparticle spacing values (λ) shown in Table 5, dual ($\alpha'/\gamma$)−$\gamma_R$ ≤ 0.10 microstructures austenitised at 0.1 °C/s (low λ) should exhibit a smaller work-hardening ability than microstructures austenitised at 10 °C/s (large λ). However, the experimental observations between the $\sigma_{YS}$ and $\sigma_{UTS}$ values in Fig. 8a show the opposite behaviour. Hence, differences in the work-hardening behaviour must originate from the changes induced in the dislocation structure during heating. Although the mutual effect of precipitation and dislocation network on the work-hardening is not well understood yet [43], it clearly affects the effective spacing between pinning points. As previously observed by TEM by the authors [29], heating at 0.1 °C/s aids the martensite recovery and leads to the rearrangement of dislocation in cells. The dislocation density within the cell walls is high, while it is low within the cell interiors, which facilitates the slip of mobile dislocations. The cell-type of dislocation structure provides a heterogeneous spatial distribution of dislocation pinning points (dislocation segment lengths), which requires a gradient of shear stresses to bow them out and produce plastic deformation [47]. This would explain the continuous yielding effect observed in the microstructures austenitised at 0.1 °C/s. Instead, the dislocation network of the CR state does not change much upon heating at 1 or 10 °C/s to temperatures slightly above $A_S$ and, thus, mainly remains in the form of dislocation forests [29]. It is suggested that the presence of dislocation forests decreases the effective obstacle spacing and, thereby, the slip

**Table 5**
Precipitates size parameters, length ($l_{ppt}$), width ($w_{ppt}$) and equivalent spherical diameter ($X$), and interparticle distance ($\lambda$) for dual ($\alpha'/\gamma$) $-\gamma_R = 0.10$ microstructures. $f_{ppt}$ represents the volume fraction of precipitates and $\Delta\sigma_{ppt}$ and $\Delta\sigma_{ss}$ stand for the precipitation and solid solution strengthening, respectively.

| HR (°C/s) | $l_{ppt}$ (nm) | $w_{ppt}$ (nm) | $X$ (nm) | $f_{ppt}$ | $\lambda$ (nm) | $\Delta\sigma_{ppt}$ (MPa) | $\Delta\sigma_{ss}$ (MPa) |
|---|---|---|---|---|---|---|---|
| 0.1 | 28 ± 11 | 11 ± 3 | 20 ± 7 | 0.07 ± 0.03 | 150 ± 66 | 574 | -99 |
| 10 | 14 ± 12 | 6 ± 4 | 10 ± 8 | 0.02 ± 0.01 | 607 ± 148 | 320 | -25 |

length of mobile dislocations in microstructures austenitised at 1 or 10 °C/s compared to microstructures austenitised at 0.1 °C/s. This is pointed as the main cause of the work-hardening ability decrease in dual ($\alpha'/\gamma$) $-\gamma_R \leq 0.10$ microstructures as the austenitisation heating rate is increased. Although the role of the austenite plastic deformation on the work-hardening should not be disregarded, it is not the factor controlling the work hardening of dual ($\alpha'/\gamma$)$-\gamma_R \leq 0.10$ microstructures.

In summary, the yield strength of dual ($\alpha'/\gamma$) microstructures obtained by heating up to temperatures slightly above $A_S$ is mainly controlled by the dislocation density inherited from the cold-rolled state and the nanoprecipitation of $Ni_3(Ti,Al)$ in martensite during heating. The martensite recovery does not adversely affect the yield strength due to the presence of nanoprecipitates; however, it plays an important role in the work-hardening ability.

*B) Increase of the austenite volume fraction and martensite recovery*.

Increasing the austenite volume fraction above 0.10 causes a continuous decay in the yield strength and tensile strength, but improves the work-hardening and the elongation. Dual ($\alpha'/\gamma$) – 0.60 microstructures exhibit comparable strength values, indicating that the strength of martensite is similar regardless of the heating rate. This behaviour corresponds to microstructures within region ② in Fig. 8a.

The *yield strength* deteriorates more significantly with the increase of the austenite volume fraction by lowering the heating rate. Since a low heating rate leads to a harder martensite through a larger volume fraction of precipitates, its strengthening contribution becomes less important as more austenite forms. Additionally, the martensite might significantly soften upon slow heating to intermediate austenitisation temperatures due to pronounced changes in the precipitation state and dislocation structure during heating. Table 2 showed, nevertheless, that the precipitate size barely changes by rising the austenitisation temperature. This resistance to coarsen of the $Ni_3(Ti,Al)$ nanoprecipitates, already observed in previous works during isothermal holding at 450–475 °C up to 72 h, is attributed to the formation of a Mo-rich film in direct contact with the $Ni_3(Ti,Al)$ precipitates in the steel under investigation [12,45]. However, why the austenitisation temperature during continuous heating seems not to increase the precipitate size is not clear yet. Therefore, the main contributor to the martensite strength loss in microstructures austenitised at 0.1 °C/s might come from a more pronounced martensite recovery compared to the microstructures austenitised at higher rates [29].

The *work-hardening* of dual ($\alpha'/\gamma$) microstructures within region ② increases continuously as the austenite volume fraction rises. These microstructures consist of metastable austenite grains of nano-scale dispersed in a martensitic matrix, which results from a high austenite nuclei density provided during heating by the high dislocation density of the CR state [29]. The microstructure is exemplified by Fig. 9, which shows a BF and a DF TEM micrographs of a dual ($\alpha'/\gamma$)$-\gamma_R = 0.60$ microstructure obtained by heating at 1 °C/s to 730 °C. The DF image reveals two austenite grains and the presence of rod-shaped precipitates within the martensite (pointed by red arrows). The continuity of the martensitic matrix rises the strength of the microstructure, while the presence of increasing volume fractions of metastable austenite grains confers with simultaneous enhanced ductility and strengthening via the mechanically-induced martensitic transformation plus the composite effect. The contribution of the martensitic transformation to the work-hardening becomes more important as the austenite volume fraction in the dual ($\alpha'/\gamma$) microstructure increases (especially above 0.30) since the austenite mechanical stability decreases (Fig. 6). Nevertheless, the extent of the martensitic transformation is lower than expected considering the mechanical driving force applied during the tensile test (as discussed in the previous section). As suggested by Fultz & Morris [48], the mechanical stability of austenite depends on the energy associate to accommodate the transformation strains by the surrounding martensite. The high hardness of the martensite due to the presence of $Ni_3(Ti,Al)$ in dual ($\alpha'/\gamma$)$-\gamma_R \leq 0.50$ microstructures might partially inhibit the $\gamma \rightarrow \alpha'$ transformation due to two possible effects: 1) the stress is not transferred to the austenite during loading since the martensitic matrix carries the main part of the stress, which was referred as "shielding" effect of the martensite by Jacques et al. [49], and 2) the volume expansion associated to the fcc-to-bcc lattice transformation is not accommodated by the surrounding martensite due to its high strength. Besides the composition and grain size, the above mentioned

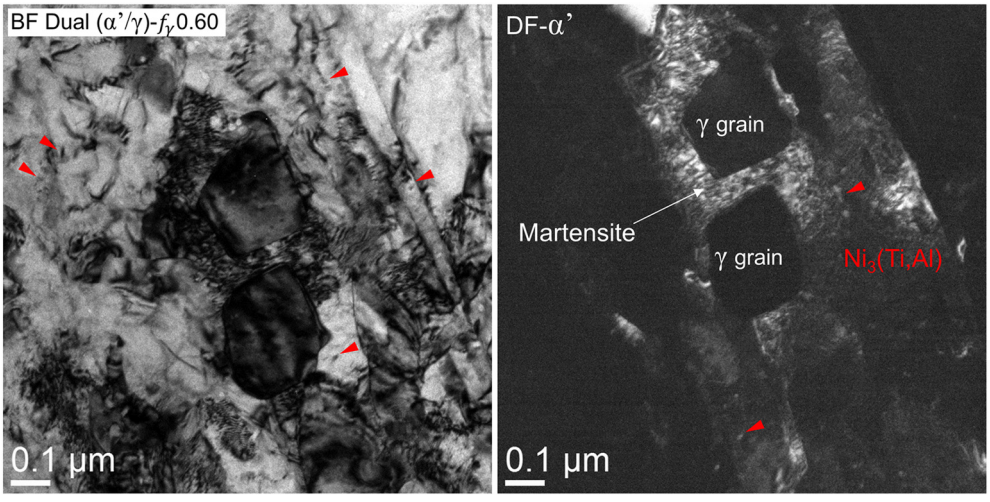


**Fig. 9.** BF and DF TEM micrographs of a dual ($\alpha'/\gamma$)$-\gamma_R = 0.60$ microstructure obtained by heating at 1 °C/s to 730 °C.

"shielding" effects might be responsible for the extra increase of the austenite stability experimentally observed in dual ($\alpha'/\gamma$)−$\gamma_R \leq 0.50$ microstructures (Fig. 6).

*4.2.2. Microstructures of austenitic matrix: the influence of grain size and χ-phase*

Fig. 8a shows a pronounced yield strength drop of about 400 MPa in dual ($\alpha'/\gamma$) microstructures when the volume fraction of austenite increases from 0.60 to 0.70. Thereafter, the yield strength remains essentially constant and the tensile strength decreases linearly with further increase of the austenite volume fraction in the microstructure. This behaviour is similar for all heating rates and corresponds to region ③ of Fig. 8a.

The *yield strength* of austenitic microstructures mainly depends on the grain-boundary strengthening, which is known as the Hall-Petch effect [18,21]:

$$\sigma_{YS}^{\gamma} = \sigma_0 + k_{HP}/\sqrt{d_\gamma} \quad (5)$$

where $k_{HP}$ is the hall-Petch coefficient, $d_\gamma$ is the austenite grain size and $\sigma_0$ is the off-set stress and contains the contributions from the solid solution, precipitation and dislocation forest: $\sigma_0 = \sigma_{ss} + \sigma_{ppt} + \sigma_\rho$. Previous investigations in similar high-alloyed austenitic stainless steel such as AISI 301, 316 L and S304H [19,20,50], have revealed Hall-Petch parameters of $\sigma_0$= 205 MPa and $k_{HP}$= 395 MPa $\mu m^{-1/2}$ for austenite grain sizes varying from 0.20 to 6.50 μm. Introducing these Hall-Petch parameters and the experimental austenite grain sizes measured for fully austenitised microstructures (360–440 nm, see Table 1) in Eq. (5) renders yield strength values in the range of 800–865 MPa, which are similar to or lower than those obtained experimentally. This confirms that the austenite grain size is the main controlling strengthening mechanism in partially and fully austenitised microstructures within region ③. The heating rate does not affect significantly the yield strength since heating to $A_F$ at rates of 0.1–10 °C/s results in similar austenite grain sizes. This also reflects that the formation of different volume fractions of χ-phase precipitates of 50–150 nm upon different heating rates (Fig. 2) barely influences neither the yield strength nor the tensile strength.

Additionally, thermodynamic calculations predict the complete dissolution of the $Ni_3$(Ti,Al) precipitates in martensite at 650 °C. Assuming that the dissolution process is shifted to higher temperatures in a similar magnitude as the $A_S$ with respect to the bcc-to-fcc equilibrium transformation temperature, the dissolution of the $Ni_3$(Ti,Al) phase should be complete in dual microstructures with austenite volume fractions of about 0.70. In contrast to microstructures within regions ① and ②, in microstructures within region ③, the predominant presence of austenite plus the martensite softening due to the complete dissolution of $Ni_3$(Ti,Al) results in the austenite phase controlling the yield strength [14]. The change of the phase controlling the yield strength from martensite to austenite is pointed as the main cause for the yield strength drop observed when the austenite volume fraction is increased from 0.60 to 0.70 (between regions ② and ③).

The *work-hardening* ability of dual ($\alpha'/\gamma$) and fully austenitised microstructures within region ③ is improved with respect to that of microstructures within region ②. The austenite, as a relatively softer phase than martensite, facilitates the plastic accommodation associated to the $\alpha' \rightarrow \gamma$ transformation and, thus, enables a larger extent of the transformation. This is the main reason for the decrease of austenite mechanical stability with the increase of austenite volume fraction observed in Fig. 6. The interaction between the plastic deformation in austenite, the formation of mechanically-induced martensite and dispersed islands of martensite creates internal stresses at the $\alpha'/\gamma$ boundaries that help to initiate plastic flow in the martensite [14]. As observed by synchrotron x-ray diffraction during in-situ uniaxial tensile loading of a TRIP-assisted duplex stainless steel [38], the point at which the most part of the load is transferred to the martensite coincides with the point at which the martensite formation rate is the highest. The load redistribution between phases takes place at this point since the martensite becomes the predominant phase in the microstructure [51]; i.e. the microstructure resembles a dual ($\alpha'/\gamma$) microstructure with a martensite matrix, and the plastic deformation in martensite contributes further to the work-hardening of the microstructure. This work-hardening mechanism appears to be optimised in dual ($\alpha'/\gamma$) $-\gamma_R = 0.70$ microstructures. The combination of phase fractions and spatial distribution gives rise to an outstanding strengthening behaviour during tensile testing through an optimum degree of mechanical stability of austenite and an efficient continuous load transfer to martensite.

The mechanical behaviour of dual ($\alpha'/\gamma$)−$\gamma_R \geq 0.70$ and fully austenitised microstructures is independent of the heating rate and, hence, of the volume fraction of χ-phase. However, the austenitisation at heating rates of 0.1 °C/s might deteriorate the corrosion resistance properties of the steel. The formation of a volume fraction of χ-phase of about 0.11 (by heating at 0.1 °C/s up to $A_F$) decreases the overall Cr content in solid solution down to 11 wt. % and, probably, to lower values in the surroundings of the precipitates. Therefore, it is recommended to use heating rates of 1 or 10 °C/s in order to minimise the precipitation of χ-phase.

## 5. Conclusions

The microstructural role in the mechanical behaviour and strengthening mechanisms of ultra-fine (UFG) grained dual ($\alpha'/\gamma$) and austenitic ($\gamma$) microstructures is investigated in a cold-rolled metastable stainless steel austenitised upon different isochronal conditions (0.1, 1 and 10 °C/s). The mechanical behaviour is influenced by: (i) the nanoprecipitation of the $Ni_3$(Ti,Al) phase in martensite, (ii) the volume fraction of austenite and martensite, (iii) the mechanical stability of austenite. A wide spectrum of strength-ductility combinations can be achieved by adjusting the microstructure based on the austenitisation temperature and heating rate, as schematically summarized in Fig. 10.

- *Martensitic matrix*. The strength of dual ($\alpha'/\gamma$) microstructures with austenite fractions of 0.60 or lower is controlled by the strength of the martensite phase, which is significantly influenced by the heating rate. Decreasing the heating rate increases the volume fraction of nanometric $Ni_3$(Ti,Al) particles and promotes the partial recovery of martensite. This nanoprecipitation rises remarkably the strength, while the recovery slightly improves the work-hardening of dual ($\alpha'/\gamma$) microstructures with small austenite fractions, with respect to the cold-rolled martensitic microstructure or the use of higher heating rates. Further increase in the austenite volume fraction causes a loss of strength but higher work-hardening abilities and larger elongations. This is attributed to the austenite mechanical stability decrease and thus to a more important contribution of the mechanically-induced martensite formation.
- *Austenitic matrix*. The mechanical behaviour of dual ($\alpha'/\gamma$) microstructures, with austenite fractions of 0.70 or higher, and fully austenitic microstructures is barely affected by the heating rate. The yield strength is mainly governed by the ultra-fine austenite grain size ($d_\gamma$) and the elongation is improved as the austenite volume fraction increases. The work-hardening is remarkably increased with respect to dual ($\alpha'/\gamma$) microstructures with a martensitic matrix due to the presence of martensite dispersed in a relatively softer austenitic matrix. This combination of phase volume fractions and spatial distribution decreases the mechanical stability of the austenite, which allows larger mechanically-induced martensite volume fractions to be formed and leads to outstanding strengthening behaviours via the composite effect.

This study provides fundamental understanding on the microstructural characteristics controlling the mechanical behaviour and stability

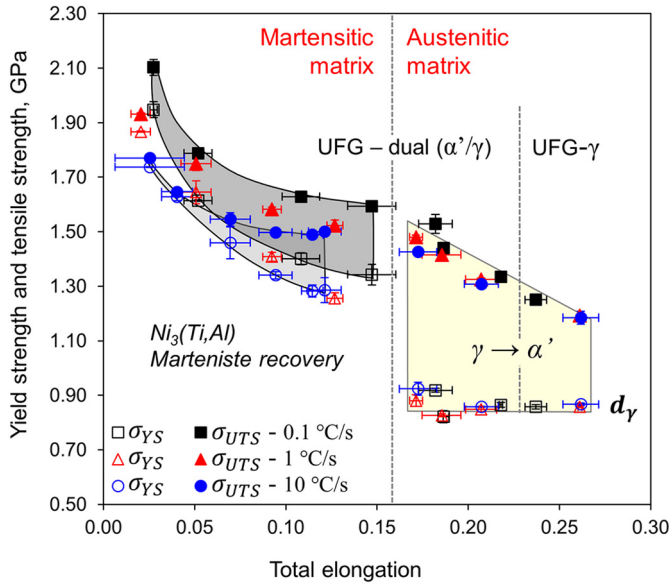


**Fig. 10.** Strength-total elongation combinations that can be achieved by ultrafine grained (UFG) dual-(α′/γ) and austenitic (γ) microstructures obtained by heating at: 0.1 (black), 1 (red) and 10 °C/s (blue). Open and solid data points represent the yield strength ($\sigma_{YS}$) and tensile strength ($\sigma_{UTS}$), respectively. Shaded grey areas highlight the influence of the heating rate on the mechanical behaviour of dual-(α′/γ) microstructures with a martensitic matrix, which are attributed to the precipitation hardening ($\sigma_{ppt}$) from the $Ni_3$(Ti,Al) phase and martensite recovery. The shaded yellow area represents the mechanical behaviour of microstructures with an austenitic matrix, which is independent on the heating rate. The yield strength is controlled by the austenite grain size ($d_\gamma$) and the γ → α′ transformation governs the work-hardening. (For interpretation of the references to colour in this figure legend, the reader is referred to the web version of this article.)

of ultrafine grained austenite/martensite microstructures in metastable stainless steels. The present results will enable the optimisation of processing routes for the design of microstructures within a broad window of mechanical properties.

## CRediT authorship contribution statement

**C. Celada-Casero:** Conceptualization, Methodology, Validation, Formal analysis, Investigation, Writing - original draft, Visualization, Funding acquisition. **B.M. Huang:** Data curation. **J.-R. Yang:** Supervision, Writing - review & editing. **D. San-Martin:** Conceptualization, Resources, Supervision, Investigation, Writing - review & editing, Project administration, Funding acquisition.

## CRediT authorship contribution statement

**C. Celada-Casero:** Conceptualization, Methodology, Validation, Formal analysis, Investigation, Writing - original draft, Visualization, Funding acquisition. **B.M. Huang:** Data curation. **J.-R. Yang:** Supervision, Writing - review & editing. **D. San-Martin:** Conceptualization, Resources, Supervision, Investigation, Writing - review & editing, Project administration, Funding acquisition.

## Acknowledgements

CCC thanks the financial support from the Consejo Superior de Investigaciones Científicas (CSIC) in the form of a JAE-predoc grant (JAEPre_2011_01167) co-funded by the European Social Fund and the National Science Council of Taiwan for granting a research internship at the National Taiwan University (NTU). CCC and DSM are grateful to dr. M. Groen and prof. J. Post, Philips Consumer Lifestyle B. V., Drachten, The Netherlands, for the material supply and fruitful discussions. The authors acknowledge the financial support from the Ministerio de Economía y Competitividad (project No. MAT2010-19522) and CAI of Physical Techniques, Complutense University of Madrid, for experimental support.

## References

[1] K.H. Lo, C.H. Shek, J.K.L. Lai, Recent developments in stainless steels, Materials Science and Engineering: R: Reports 65 (2009) 39–104.
[2] P. Liu, Relationships between microstructure and properties of stainless steels— a few working examples, Mater. Charact. 44 (2000) 413–424.
[3] E.S. Perdahcıoğlu, H.J.M. Geijselaers, J. Huétink, Influence of stress state and strain path on deformation induced martensitic transformations, Mater. Sci. Eng. A 481-482 (2008) 727–731.
[4] J. Post, H. Nolles, K. Datta, H.J.M. Geijselaers, Experimental determination of the constitutive behaviour of a metastable austenitic stainless steel, Mater. Sci. Eng. A 498 (2008) 179–190.
[5] C. Celada Casero, D. San Martín, Austenite formation in a cold-rolled semi-austenitic stainless steel, Metall Mater Trans A 45 (2014) 1767–1777.
[6] D.S. Martin, N.H. van Dijk, E. Brück, S. van der Zwaag, The isothermal martensite formation in a maraging steel: a magnetic study, Mater. Sci. Eng. A 481-482 (2008) 757–761.
[7] D. San Martin, N.H. van Dijk, E. Jiménez-Melero, E. Kampert, U. Zeitler, S. van der Zwaag, Real-time martensitic transformation kinetics in maraging steel under high magnetic fields, Mater. Sci. Eng. A 527 (2010) 5241–5245.
[8] D. San Martin, E. Jimenez-Melero, J.A. Duffy, V. Honkimaki, S. van der Zwaag, N.H. van Dijk, Real-time synchrotron X-ray diffraction study on the isothermal martensite transformation of maraging steel in high magnetic fields, J. Appl. Crystallogr. 45 (2012) 748–757.
[9] K. Stiller, M. Hättestrand, F. Danoix, Precipitation in 9Ni–12Cr–2Cu maraging steels, Acta Mater. 46 (1998) 6063–6073.
[10] E.V. Pereloma, A. Shekhter, M.K. Miller, S.P. Ringer, Ageing behaviour of an Fe–20Ni–1.8Mn–1.6Ti–0.59Al (wt%) maraging alloy: clustering, precipitation and hardening, Acta Mater. 52 (2004) 5589–5602.
[11] M. Thuvander, M. Andersson, K. Stiller, Precipitation process of martensitic PH stainless steel Nanoflex, Mater Sci Tech 28 (2012) 695–701.
[12] C. Celada-Casero, J. Chao, E. Urones-Garrote, D. San Martin, Continuous hardening during isothermal aging at 723 K (450 °C) of a precipitation hardening stainless steel, Metall Mater Trans A 47 (2016) 5280–5287.
[13] M. Eskandari, A. Najafizadeh, A. Kermanpur, M. Karimi, Potential application of nanocrystalline 301 austenitic stainless steel in lightweight vehicle structures, Mater. Des. 30 (2009) 3869–3872.
[14] Y. Tomota, K. Kuroki, T. Mori, I. Tamura, Tensile deformation of two-ductile-phase alloys: flow curves of α-γ Fe·Cr·Ni alloys, Mater. Sci. Eng. 24 (1976) 85–94.
[15] P. Shina, K. Tharian, K. Sreekumar, K. Nagarajan, D. Sarma, Effect of aging on microstructure and mechanical properties of cobalt free 18%Ni (250 grade) maraging steel, Mater Sci Tech 14 (1998) 1–9.
[16] R. Schnitzer, S. Zinner, H. Leitner, Modeling of the yield strength of a stainless maraging steel, Scripta Mater 62 (2010) 286–289.
[17] E.I. Galindo-Nava, W.M. Rainforth, P.E.J. Rivera-Díaz-del-Castillo, Predicting microstructure and strength of maraging steels: elemental optimisation, Acta Mater. 117 (2016) 270–285.
[18] C.X. Huang, G. Yang, C. Wang, Z.F. Zhang, S.D. Wu, Mechanical behaviors of ultrafine-grained 301 austenitic stainless steel produced by equal-channel angular pressing, Metall Mater Trans A 42 (2011) 2061–2071.
[19] I. Shakhova, V. Dudko, A. Belyakov, K. Tsuzaki, R. Kaibyshev, Effect of large strain cold rolling and subsequent annealing on microstructure and mechanical properties of an austenitic stainless steel, Mater. Sci. Eng. A 545 (2012) 176–186.
[20] G. Dini, A. Najafizadeh, R. Ueji, S.M. Monir-Vaghefi, Tensile deformation behavior of high manganese austenitic steel: the role of grain size, Mater. Des. 31 (2010) 3395–3402.
[21] S. Rajasekhara, P.J. Ferreira, L.P. Karjalainen, A. Kyröläinen, Hall–Petch behavior in ultra-fine-grained AISI 301LN stainless steel, Metall Mater Trans A 38 (2007) 1202–1210.
[22] A. Järvenpää, M. Jaskari, J. Man, L.P. Karjalainen, Austenite stability in reversion-treated structures of a 301LN steel under tensile loading, Mater. Charact. 127 (2017) 12–26.
[23] G. Fargas, J.J. Roa, A. Mateo, Effect of shot peening on metastable austenitic stainless steels, Mater. Sci. Eng. A 641 (2015) 290–296.
[24] F. Maqbool, R. Hajavifard, F. Walther, M. Bambach, Engineering the residual stress state of the metastable austenitic stainless steel (MASS) disc springs by incremental sheet forming (ISF), Prod. Eng. 13 (2019) 139–148.
[25] G. Fargas, A. Zapata, J.J. Roa, I. Sapezanskaia, A. Mateo, Correlation between microstructure and mechanical properties before and after reversion of metastable austenitic stainless steels, Metall Mater Trans A 46 (2015) 5697–5707.
[26] M. Naghizadeh, H. Mirzadeh, Microstructural evolutions during reversion annealing of cold-rolled AISI 316 austenitic stainless steel, Metall Mater Trans A 49 (2018) 2248–2256.
[27] D. Raabe, D. Ponge, O. Dmitrieva, B. Sander, Nanoprecipitate-hardened 1.5 GPa steels with unexpected high ductility, Scripta Mater 60 (2009) 1141–1144.
[28] C. Celada, I. Toda-Caraballo, B. Kim, D. San Martín, Chemical banding revealed by chemical etching in a cold-rolled metastable stainless steel, Mater. Charact. 84 (2013) 142–152.
[29] C. Celada-Casero, B.M. Huang, M.M. Aranda, J.R. Yang, D. San-Martin, Mechanisms of ultrafine-grained austenite formation under different isochronal conditions in a cold-rolled metastable stainless steel, Mater. Charact. 118 (2016) 129–141.

[30] D. San Martin, P.E.J. Rivera Diaz del Castillo, E. Peekstok, S. van der Zwaag, A new etching route for revealing the austenite grain boundaries in an 11.4% Cr precipitation hardening semi-austenitic stainless steel, Mater. Charact. 58 (2007) 455–460.
[31] C.A. Schneider, W.S. Rasband, K.W. Eliceiri, NIH image to ImageJ: 25 years of image analysis, Nat. Methods 9 (2012) 671.
[32] J. Han, Y.-K. Lee, The effects of the heating rate on the reverse transformation mechanism and the phase stability of reverted austenite in medium Mn steels, Acta Mater. 67 (2014) 354–361.
[33] H. Leitner, M. Schober, R. Schnitzer, Splitting phenomenon in the precipitation evolution in an Fe–Ni–Al–Ti–Cr stainless steel, Acta Mater. 58 (2010) 1261–1269.
[34] J.S. Kasper, The ordering of atoms in the chi-phase of the iron-chromium-molybdenum system, Acta Metall. 2 (1954) 456–461.
[35] R. Blondé, E. Jimenez-Melero, L. Zhao, J.P. Wright, E. Brück, S. van der Zwaag, et al., Mechanical stability of individual austenite grains in TRIP steel studied by synchrotron X-ray diffraction during tensile loading, Mater. Sci. Eng. A 618 (2014) 280–287.
[36] G.B. Olson, M. Cohen, A general mechanism of martensitic nucleation: part II. FCC → BCC and other martensitic transformations, Metall. Trans. A. 7 (1976) 1905–1914.
[37] J.H. Ryu, D.-I. Kim, H.S. Kim, H.K.D.H. Bhadeshia, D.-W. Suh, Strain partitioning and mechanical stability of retained austenite, Scripta Mater 63 (2010) 297–299.
[38] Y. Tian, S. Lin, J.Y.P. Ko, U. Lienert, A. Borgenstam, P. Hedström, Micromechanics and microstructure evolution during in situ uniaxial tensile loading of TRIP-assisted duplex stainless steels, Mater. Sci. Eng. A 734 (2018) 281–290.
[39] J.R. Patel, M. Cohen, Criterion for the action of applied stress in the martensitic transformation, Acta Metall. 1 (1953) 531–538.
[40] G.B. Olson, K. Tsuzaki, M. Cohen, Statistical aspects of martensitic nucleation, MRS Proc. 57 (2011) 129.
[41] H.J.M. Geijselaers, E.S. Perdahcıoğlu, Mechanically induced martensitic transformation as a stress-driven process, Scripta Mater 60 (2009) 29–31.
[42] E.S. Perdahcıoğlu, H.J.M. Geijselaers, A macroscopic model to simulate the mechanically induced martensitic transformation in metastable austenitic stainless steels, Acta Mater. 60 (2012) 4409–4419.
[43] F. Roters, D. Raabe, G. Gottstein, Work hardening in heterogeneous alloys—a microstructural approach based on three internal state variables, Acta Mater. 48 (2000) 4181–4189.
[44] S. Takaki, K.-L. Ngo-Huynh, N. Nakada, T. Tsuchiyama, Strengthening mechanism in ultra low carbon martensitic steel, ISIJ Int. 52 (2012) 710–716.
[45] M. Thuvander, M. Andersson, K. Stiller, Atom probe tomography investigation of lath boundary segregation and precipitation in a maraging stainless steel, Ultramicroscopy 132 (2013) 265–270.
[46] T. Gladman, Precipitation hardening in metals, Mater Sci Tech 15 (1999) 30–36.
[47] Z. Arechabaleta, P. van Liempt, J. Sietsma, Unravelling dislocation networks in metals, Mater. Sci. Eng. A 710 (2018) 329–333.
[48] B. Fultz, J.W. Morris, The mechanical stability of precipitated austenite in 9Ni steel, Metall. Trans. A. 16 (1985) 2251–2256.
[49] P.J. Jacques, F. Delannay, J. Ladrière, On the influence of interactions between phases on the mechanical stability of retained austenite in transformation-induced plasticity multiphase steels, Metall Mater Trans A 32 (2001) 2759–2768.
[50] A. Di Schino, I. Salvatori, J.M. Kenny, Effects of martensite formation and austenite reversion on grain refining of AISI 304 stainless steel, J. Mater. Sci. 37 (2002) 4561–4565.
[51] C. Celada-Casero, H. Kooiker, M. Groen, J. Post, D. San-Martin, In-situ investigation of strain-induced martensitic transformation kinetics in an austenitic stainless steel by inductive measurements, Metals 7 (2017) 271.